Assessment of the Frequency-Domain Multi-Distance Method to Evaluate the Brain Optical Properties: Monte Carlo Simulations from Neonate to Adult

Assessment of the frequency-domain multi-distance method to evaluate the brain optical properties: Monte Carlo simulations from neonate to adult

Mathieu Dehaes,[1,*] **P. Ellen Grant,**[1,2] **Danielle D. Sliva,**[1] **Nadège Roche-Labarbe,**[2] **Rudolph Pienaar,**[1] **David A. Boas,**[2] **Maria Angela Franceschini,**[2] **and Juliette Selb**[2]

[1]*Fetal-Neonatal Neuroimaging & Development Science Center, Children's Hospital Boston and Harvard Medical School, Boston, Massachusetts 02115, USA*
[2]*Athinoula A. Martinos Center for Biomedical Imaging, Massachusetts General Hospital and Harvard Medical School, Charlestown, Massachusetts 02129, USA*
**mathieu.dehaes@childrens.harvard.edu*

Abstract: The near infrared spectroscopy (NIRS) frequency-domain multi-distance (FD-MD) method allows for the estimation of optical properties in biological tissue using the phase and intensity of radiofrequency modulated light at different source-detector separations. In this study, we evaluated the accuracy of this method to retrieve the absorption coefficient of the brain at different ages. Synthetic measurements were generated with Monte Carlo simulations in magnetic resonance imaging (MRI)-based heterogeneous head models for four ages: newborn, 6 and 12 month old infants, and adult. For each age, we determined the optimal set of source-detector separations and estimated the corresponding errors. Errors arise from different origins: methodological (FD-MD) and anatomical (curvature, head size and contamination by extra-cerebral tissues). We found that the brain optical absorption could be retrieved with an error between 8–24% in neonates and infants, while the error increased to 19–44% in adults over all source-detector distances. The dominant contribution to the error was found to be the head curvature in neonates and infants, and the extra-cerebral tissues in adults.

OCIS codes: (170.3660) Light propagation in tissues; (110.3080) Infrared imaging; (170.5280) Photon migration.

References and links

1. Y. Honda, E. Nakato, Y. Otsuka, S. Kanazawa, S. Kojima, M. Yamaguchi, and R. Kakigi, "How do infants perceive scrambled face?: A near-infrared spectroscopic study," Brain Res. **1308**, 137–146 (2010).
2. T. Wilcox, H. Bortfeld, R. Woods, E. Wruck, and D. Boas, "Hemodynamic response to featural changes in the occipital and inferior temporal cortex in infants: a preliminary methodological exploration," Dev. Sci. **11**(3), 361–370 (2008).
3. T. Karen, G. Morren, D. Haensse, A. Bauschatz, H. Bucher, and M. Wolf, "Hemodynamic response to visual stimulation in newborn infants using functional near-infrared spectroscopy," Hum. Brain Mapp. **29**, 453–460 (2008).
4. A. Gibson, T. Austin, N. Everdell, M. Schweiger, S. Arridge, J. Meek, J. Wyatt, D. Delpy, and J. Hebden, "Three-dimensional whole-head optical tomography of passive motor evoked responses in the neonate," Neuroimage **30**(2), 521–528 (2006).

#137543 - $15.00 USD Received 2 Nov 2010; revised 3 Feb 2011; accepted 4 Feb 2011; published 11 Feb 2011

5. K. Kotilahti, I. Nissilä, T. Näsi, L. Lipiäinen, T. Noponen, P. Meriläinen, M. Huotilainen, and V. Fellman, "Hemodynamic responses to speech and music in newborn infants," Hum. Brain Mapp. **31**(4), 595–603 (2010).
6. P. Zaramella, F. Freato, A. Amigoni, S. Salvadori, P. Marangoni, A. Suppjei, B. Schiavo, and L. Chiandetti, "Brain auditory activation measured by near-infrared spectroscopy (NIRS) in neonates," Pediatr. Res. **49**(2), 213–219 (2001).
7. M. Schecklmann, A. Ehlis, M. Plichta, and A. Fallgatter, "Functional near-infrared spectroscopy: a long-term reliable tool for measuring brain activity during verbal fluency," Neuroimage **43**(1), 147–155 (2008).
8. H. Bortfeld, E. Fava, and D. Boas, "Identifying cortical lateralization of speech processing in infants using near-infrared spectroscopy," Dev. Neuropsychol. **34**(1), 52–65 (2009).
9. S. Fantini, D. Hueber, M. Franceschini, E. Gratton, W. Rosenfeld, P. Stubblefield, D. Maulik, and M. Stankovic, "Non-invasive optical monitoring of the newborn piglet brain using continuous-wave and frequency-domain spectroscopy," Phys. Med. Biol. **44**(6), 1543–1563 (1999).
10. M. Franceschini, S. Thaker, G. Themelis, K. Krishnamoorthy, H. Bortfeld, S. Diamond, D. Boas, K. Arvin, and P. Grant, "Assessment of infant brain development with frequency-domain near-infrared spectroscopy," Pediatr. Res. **61**(5), 546–551 (2007).
11. N. Roche-Labarbe, S. Carp, A. Surova, M. Patel, D. Boas, P. Grant, and M. Franceschini, "Noninvasive optical measures of CBV, StO(2), CBF index, and rCMRO(2) in human premature neonates' brains in the first six weeks of life," Hum. Brain Mapp. **31**(3), 341–352 (2010).
12. P. Grant, N. Roche-Labarbe, A. Surova, G. Themelis, J. Selb, E. Warren, K. Krishnamoorthy, D. Boas, and M. Franceschini, "Increased cerebral blood volume and oxygen consumption in neonatal brain injury," J. Cereb. Blood Flow Metab. **29**(10), 1704–1713 (2009).
13. S. Arridge, M. Cope, and D. Delpy, "The theoretical basis for the determination of optical pathlengths in tissue : Temporal and frequency analysis," Phys. Med. Biol. **37**(7), 1531–1560 (1992).
14. G. Naulaers, G. Morren, S. V. Huffel, P. Casaer, and H. Devlieger, "Cerebral tissue oxygenation index in very premature infants," Arch. Dis. Child Fetal Neonatal Ed. **87**(3), F189–F192 (2002).
15. T. Leung, I. Tachtsidis, M. Smith, D. Delpy, and C. Elwell, "Measurement of the absolute optical properties and cerebral blood volume of the adult human head with hybrid differential and spatially resolved spectroscopy," Phys. Med. Biol. **51**(3), 703–717 (2006).
16. G. Pichler, K. Grossauer, E. Peichl, A. Gaster, A. Berghold, G. Schwantzer, H. Zotter, W. Mller, and B. Urlesberger, "Combination of different noninvasive measuring techniques: a new approach to increase accuracy of peripheral near infrared spectroscopy," J. Biomed. Opt. **14**(1), 014014 (2009).
17. M. Patterson, B. Chance, and B. Wilson, "Time resolved reflectance and transmittance for the non-invasive measurement of tissue optical properties," Appl. Opt. **28**(12), 2331–2336 (1989).
18. S. Fantini, M. Franceschini, J. Maier, S. Walker, B. Barbieri, and E. Gratton, "Frequency-domain multichannel optical detector for non-invasive tissue spectroscopy and oximetry," Opt. Eng. **34**, 32–42 (1995).
19. S. Matcher, "Closed-form expressions for obtaining the absorption and scattering coefficients of a turbid medium with time-resolved spectroscopy," Appl. Opt. **36**(31), 8298–302 (1997).
20. A. Liebert, H. Wabnitz, D. Grosenick, M. Möller, R. Macdonald, and H. Rinneberg, "Evaluation of optical properties of highly scattering media by moments of distributions of times of flight of photons," Appl Opt. **42**(28), 5785–5792 (2003).
21. V. Ntziachristos and B. Chance, "Accuracy limits in the determination of absolute optical properties using time-resolved NIR spectroscopy," Med. Phys. **28**(6), 1115–1124 (2001).
22. A. Pifferi, A. Torricelli, P. Taroni, and R. Cubeddu, "Reconstruction of absorber concentrations in a two-layer structure by use of multidistance time-resolved reflectance spectroscopy," Opt. Lett. **26**(24), 1963–1965 (2001).
23. J. Swartling, J. Dam, and S. Andersson-Engels, "Comparison of spatially and temporally resolved diffuse-reflectance measurement systems for determination of biomedical optical properties," Appl. Opt. **42**(22), 4612–4620 (2003).
24. F. Martelli, S. D. Bianco, G. Zaccanti, A. Pifferi, A. Torricelli, A. Bassi, P. Taroni, and R. Cubeddu, "Phantom validation and in vivo application of an inversion procedure for retrieving the optical properties of diffusive layered media from time-resolved reflectance measurements," Opt. Lett. **29**(17), 2037–2039 (2004).
25. C. Abrahamsson, T. Svensson, S. Svanberg, S. Andersson-Engels, J. Johansson, and S. Folestad, "Time and wavelength resolved spectroscopy of turbid media using light continuum generated in a crystal fiber," Opt. Express **12**(17), 4103–4112 (2004).
26. A. Pifferi, A. Torricelli, A. Bassi, R. Cubeddu, H. Wabnitz, D. Grosenick, M. Mller, R. Macdonald, J. Swartling, T. Svensson, S. Andersson-Engels, R. van Veen, H. Sterenborg, J. Tualle, H. Nghiem, S. Avrillier, M. Whelan, and H. Stamm, "Performance assessment of photon migration instruments: the MEDPHOT protocol," Appl. Opt. **44**(11), 2104–2114 (2005).
27. J. Selb, D. Joseph, and D. Boas, "Time-gated optical system for depth-resolved functional brain imaging," J. Biomed. Opt. **11**(4), 044008 (2006).
28. L. Gagnon, C. Gauthier, R. Hoge, F. Lesage, J. Selb, and D. Boas, "Double-layer estimation of intra- and extracerebral hemoglobin concentration with a time-resolved system," J. Biomed. Opt. **13**(5), 054019 (2008).
29. S. Ijichi, T. Kusaka, K. Isobe, K. Okubo, K. Kawada, M. Namba, H. Okada, T. Nishida, T. Imai, and S. Itoh, "De-

#137543 - $15.00 USD Received 2 Nov 2010; revised 3 Feb 2011; accepted 4 Feb 2011; published 11 Feb 2011

velopmental changes of optical properties in neonates determined by near-infrared time-resolved spectroscopy," Pediatr. Res. **58**, 568–573 (2005).
30. J. Zhao, H. Ding, X. Hou, C. Zhou, and B. Chance, "In vivo determination of the optical properties of infant brain using frequency-domain near-infrared spectroscopy," J. Biomed. Opt. **10**, 024028 (2005).
31. J. Choi, M. Wolf, V. Toronov, U. Wolf, C. Polzonetti, D. Hueber, L. Safonova, R. Gupta, A. Michalos, W. Mantulin, and E. Gratton, "Noninvasive determination of the optical properties of adult brain: near-infrared spectroscopy approach," J. Biomed. Opt. **9**(1), 221–229 (2004).
32. D. Comelli, A. Bassi, A. Pifferi, P. Taroni, A. Torricelli, R. Cubeddu, F. Martelli, and G. Zaccanti, "In vivo time-resolved reflectance spectroscopy of the human forehead," Appl. Opt. **46**(10), 1717–1725 (2007).
33. E. Ohmae, Y. Ouchi, M. Oda, T. Suzuki, S. Nobesawa, T. Kanno, E. Yoshikawa, M. Futatsubashi, Y. Ueda, H. Okada, and Y. Yamashita, "Cerebral hemodynamics evaluation by near-infrared time-resolved spectroscopy: correlation with simultaneous positron emission tomography measurements," Neuroimage **29**(3), 697–705 (2006).
34. A. Kienle, M. Patterson, N. Dgnitz, R. Bays, G. Wagnires, and H. van den Bergh, "Noninvasive Determination of the Optical Properties of Two-Layered Turbid Media," Appl. Opt. **37**(4), 779–791 (1998).
35. F. Martelli, A. Sassaroli, S. D. Bianco, and G. Zaccanti, "Solution of the time-dependent diffusion equation for a three-layer medium: application to study photon migration through a simplified adult head model," Phys. Med. Biol. **52**(10), 2827–2843 (2007).
36. A. Barnett, J. Culver, A. Sorensen, A. Dale, and D. Boas, "Robust inference of baseline optical properties of the human head with three-dimensional segmentation from magnetic resonance imaging," Appl. Opt. **42**, 3095–3108 (2003).
37. D. Boas, J. Culver, J. Scott, and A. Dunn, "Three dimensional Monte Carlo code for photon migration through complex heterogeneous media including the adult human head," Opt. Express **10**(3), 159–170 (2002).
38. G. Strangman, M. Franceschini, and D. Boas, "Factors affecting the accuracy of near-infrared spectroscopy concentration calculations for focal changes in oxygenation parameters," Neuroimage **18**(4), 865–879 (2003).
39. S. Prahl, "Optical Absorption of Hemoglobin," `http://omlcogiedu/spectra/hemoglobin/summaryhtml` (2002).
40. A. Yaroslavsky, I. Yaroslavsky, T. Goldbach, and H.-J. Schwarzmaier, "Optical properties of blood in the near-infrared spectral range," Proc SPIE **2678**, 314–324 (1996).
41. S. Fantini, M. Franceschini, and E. Gratton, "Semi-infinite-geometry boundary problem for light migration in highly scattering media: a frequency-domain study in the diffusion approximation," J. Opt. Soc. Am. B **11**(10), 2128–2138 (1994).
42. S. Fantini, M. Franceschini, J. Fishkin, B. Barbieri, and E. Gratton, "Quantitative determination of the absorption spectra of chromophores in strongly scattering media: a light-emitting-diode based technique," Appl. Opt. **33**(22), 5204–5213 (1994).
43. S. Meyer, *Data Analysis for Scientists and Engineers*, (Wiley, 1975).
44. J. Heiskala, T. Neuvonen, P. Grant, and I. Nissilä, "Significance of tissue anisotropy in optical tomography of the infant brain," Appl. Opt. **46**(10), 1633–1640 (2007).
45. Q. Fang, "Mesh-based Monte Carlo method using fast ray-tracing in Plücker coordinates," Biomed. Opt. Express **1**(1), 165–175 (2010).

1. Introduction

Near-infrared spectroscopy (NIRS) measures the attenuation of diffuse near-infrared light (650–950 nm) propagating through biological tissues at two or more wavelengths, allowing for the characterization of the two main chromophores in this spectral window: oxygenated hemoglobin (HbO) and reduced hemoglobin (HbR). Therefore, NIRS is highly sensitive to tissue vascularization and oxygenation, making it an ideal tool for cerebral monitoring and imaging. Applications to functional brain imaging have spanned a diverse range of studies, including visual [1–3], sensori-motor [4], auditory [5, 6], and cognitive [7, 8] tasks. While in this context of functional imaging NIRS measures the hemodynamic *changes* associated with brain activation, the determination of the *absolute* optical absorption of the brain, directly related to baseline hemoglobin concentrations, is a more challenging application [9, 10]. Such quantitative absolute measurements are of considerable interest for longitudinal and cross-sectional studies, allowing comparison of cerebral oxygenation and blood volume between subjects, as well as monitoring within a subject over time, opening the door to a number of diagnostic and treatment monitoring applications [11, 12].

The most commonly used modality for functional NIRS, the continuous-wave (CW) ap-

#137543 - $15.00 USD Received 2 Nov 2010; revised 3 Feb 2011; accepted 4 Feb 2011; published 11 Feb 2011

proach, is not suited for absolute characterization of tissue optical properties, because it cannot distinguish between the absorption μ_a and scattering μ_s' of a medium [13]. Some publications have nonetheless presented CW estimates of baseline optical properties of tissues [14–16]. However they either report a tissue oxygenation index (TOI) [14, 16], which is the product $\mu_s' \times \mu_a$, or they require that oxygen saturation be varied within a physiological range through such manipulations as hypoxic events [15] which ethically cannot be performed in infants.

Unlike CW measurements, NIRS in the time-domain (TD) and frequency-domain (FD) allows for the characterization of the baseline μ_a and μ_s' of a biological tissue [17–20] without inducing changes in saturation, or making assumptions about μ_s'. Pulsed (TD method) or radiofrequency modulated (FD method) light is injected into the medium and its detection provides information about mean time of flights of photons (TD method) or phase shift (FD method), both related to μ_s'. The commonly used FD multi-distance (FD-MD) method takes advantage of the phase shift and attenuation of modulated light at several distances to retrieve the baseline optical properties of the medium assumed homogeneous [18]. These TD and FD methods have been validated with simulations, phantom experiments and animal studies [21–28]. *In vivo* applications of baseline measurements of the optical properties of the human brain include studies in premature and term neonates and infants [10–12, 29, 30], as well as adults [28, 31–33]. For example, our group has applied the FD-MD method on a large scale to the study of healthy brain development in term and pre-term infants during the first year of life [10, 11], as well as to the assessment of brain injury in a neonatal population [12].

With the exception of a few studies, most approaches rely on a homogeneous semi-infinite model of the head because of its simplicity. However this lack of realism introduces error in the recovered optical properties. Two- [22, 24, 28, 34] or three-layer [35] geometries have been suggested instead, as well as more realistic brain structure obtained from magnetic resonance imaging (MRI) segmentation [36], but practical applications remain challenging. In newborns the measurement can be influenced by the presence of a thick low-scattering CSF layer, as well as the small head size and the stronger curvature of the head's surface. In adults, the main challenge is the thickness of the extra-cerebral layers, which can reach more than 1 cm. No systematic study of these effects has been published to our knowledge. Validation studies are difficult to perform because there is no access to actual cerebral absorption values in humans.

In the present study, our aim was to use Monte Carlo simulations to systematically investigate the accuracy of the FD-MD method for retrieving brain absorption coefficients using a semi-infinite homogeneous model with a range of age groups, from the newborn to the adult.

2. Methods

2.1. Simulated measurements: Monte Carlo approach

Realistic data were generated using a 3D Monte Carlo (MC) code [37], modeling the photon propagation in head segmentations obtained from MRI scans.

2.1.1. Head models

We simulated data sets for four different ages: a term newborn of 38 weeks gestational age, 6 and 12 month (mo.) old infants, and an adult. A realistic 3D head model was obtained from each data set by segmentation of an MR T1 scan into four tissue types (see Fig. 1): white matter (WM), gray matter (GM), cerebrospinal fluid (CSF) and a superficial layer (superf) comprising scalp and skull. The voxel size was 1.0 mm in all directions for all head models. Figure 1 shows 3D views and axial slices of the segmented heads at each age. Gray and white matter were subsequently combined into a single "brain" tissue type with identical optical properties [38].

The effect of extra-cerebral inhomogeneities was investigated by simulating a blood vessel in the scalp of the adult. Located parallel to the optical probe at a depth of 4 to 6 mm from the

#137543 - $15.00 USD Received 2 Nov 2010; revised 3 Feb 2011; accepted 4 Feb 2011; published 11 Feb 2011

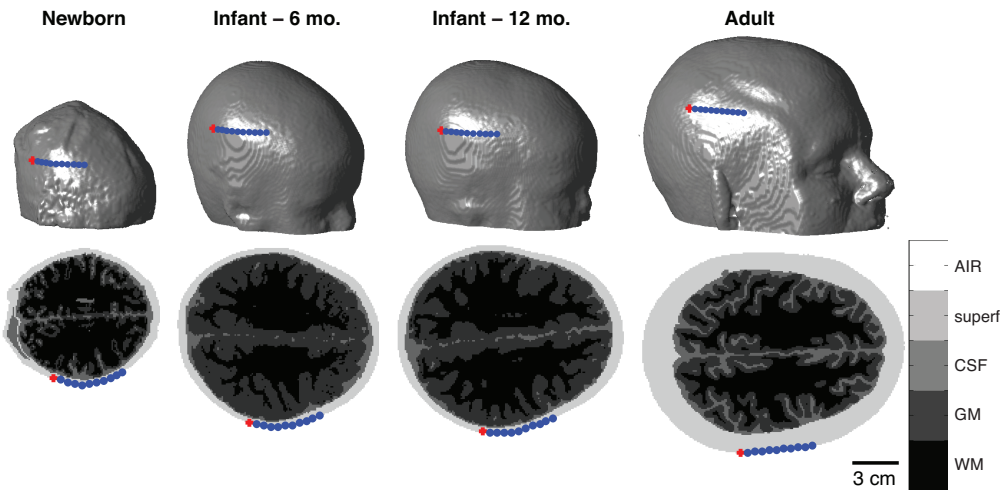

Fig. 1. Segmented head models: 3D and 2D axial views. Segmentations consist of 4 tissue types: superficial layers (superf) of scalp and skull, CSF, gray matter (GM), and white matter (WM). Sources and detectors are represented by red crosses and blue dots respectively. The black bar (3 cm) in the bottom right of the image indicates the scale of all 2D slices.

surface of the skin, the vessel was 30 mm long and had a diameter of 2 mm.

Table 1. Optical properties of tissue types selected for the Monte Carlo simulations

Tissue	n	g	μ_s' [cm^{-1}]	μ_a [cm^{-1}]
superf	1.3	0.01	5	$[0.1, 0.2]$
	1.3	0.01	10	$[0.1, 0.2]$
brain	1.3	0.01	10	$[0.05, 0.06, \ldots, 0.29, 0.3]$
CSF	1.3	0.01	0.1	0.04
	1.3	0.01	10	$[0.05, 0.06, \ldots, 0.29, 0.3]$

2.1.2. Optical properties

The optical properties of the scalp, skull and brain vary widely in the literature depending on the method of measurement [28–33]. *Ex-vivo* and *post-mortem* values are bound to differ significantly from *in-vivo* data due to changes in blood content. To simulate realistic absorption values, we considered a wide range of hemoglobin concentrations spanning those found in the literature (between 40 and 120 μM total hemoglobin) and converted them into absorption coefficients using tabulated values for the extinction coefficients of HbO and HbR [39]. This hemoglobin range yielded brain absorption coefficient between 0.05 and 0.3 cm^{-1}, while superficial absorption was set to 0.1 and 0.2 cm^{-1}. The absorption coefficient of the scalp blood vessel described in section 2.1.1 was set to 5 cm^{-1}, a typical value for whole blood absorption in the NIR spectrum [40]. Some studies report higher scattering in the brain than in the superficial tissues [31–33], while others present the opposite result [28], accompanied with inter-individual variability [30, 32]. For simplicity, the reduced scattering coefficient μ_s' was fixed at 10 cm^{-1} in the brain. The value of μ_s' in the superficial layer was set successively to 10 cm^{-1} and 5 cm^{-1}, to evaluate the effect of a spatial variation between tissues. The CSF was either considered part of the brain, with the same absorption and scattering coefficients, or, more realistically, as a

#137543 - $15.00 USD Received 2 Nov 2010; revised 3 Feb 2011; accepted 4 Feb 2011; published 11 Feb 2011

relatively clear medium with low absorption and scattering coefficients $\mu_a = 0.04\,\mathrm{cm}^{-1}$ and $\mu_s' = 0.1\,\mathrm{cm}^{-1}$. The refractive index n was set to 1.3, and the anisotropy coefficient g to 0.01 in all tissue types (the MC code does not accept a null value for g; see Table 1).

2.1.3. Probe geometry

Measurements were modeled from one source seen by four detectors positioned in a straight line, with 5 mm between successive detectors, as in a common FD-MD configuration. To test the effect of different groups of source-detector separations (SDs), a total of 10 detectors located every 5 mm were used and subsequently analyzed in subsets of four detectors, yielding 7 different probe configurations. The probe was positioned over the right parietal area (right and left parietal for the newborn) where the head surface is relatively flat (Fig. 1). The 1 mm voxelization of the heads creates a degree of "stair" effect in the curved regions, leading to artefacts in the simulated data, especially at short distances. To reduce this effect, 5 different probe locations within a small neighborhood (2 mm radius) were simulated and averaged together.

2.1.4. Monte Carlo simulations

The MC code has been described in details by Boas *et al.* [37]. FD measurements were simulated at a modulation frequency of 110 MHz, and the phase and modulated intensity were computed at each detector. 500 million photon packets were launched for each simulation, which took between 8 and 16 hours depending on the number of voxels included in the head.

2.2. Noise modeling

The large number of photons propagated in the MC simulations yields measurements with a very high signal to noise ratio, unrepresentative of actual experimental data. Therefore, measurements generated from MC simulations were modified by the addition of a Gaussian random noise. From each MC simulation data set of phase and intensity, we created 150 noisy measurements by adding 150 different values of phase and intensity noises. The variance of the phase and intensity noises were based on realistic values obtained experimentally with a FD instrument (Imagent, ISS Inc.) in neonates [10, 11] (noise data not published). The noise to signal ratio increases as the source-detector separation increases, for both intensity (1.6% to 4.6%) and phase (0.02% to 3.7%) from 0.5 to 5 cm, respectively. The standard deviation of the retrieved absorption coefficients over the 150 values of noise gives a realistic estimate of uncertainty due to both instrumental and physiological noises.

2.3. Optical properties recovery

The estimation of brain optical properties from simulated data was conducted using the homogeneous FD-MD method described previously [9, 18]. Briefly, in a semi-infinite homogeneous medium, the phase φ and natural logarithm of the modulated intensity of light I_{AC} vary linearly with source-detector separation d such that

$$\ln\left(d^2 I_{\mathrm{AC}}\right) = d\,S_{\mathrm{AC}} + C_{\mathrm{AC}} \qquad \text{and} \qquad \varphi = d\,S_\varphi + C_\varphi \tag{1}$$

where S_{AC} and S_φ are the slopes and C_{AC} and C_φ are the y-intercepts of the linear regressions. Absorption and reduced scattering coefficients of the homogeneous model can then be estimated by

$$\mu_a = \frac{\omega}{2v}\left(\frac{S_\varphi}{S_{\mathrm{AC}}} - \frac{S_{\mathrm{AC}}}{S_\varphi}\right) \qquad \text{and} \qquad \mu_s' = \frac{S_{\mathrm{AC}}^2 - S_\varphi^2}{3\mu_a} - \mu_a \tag{2}$$

where ω is the angular modulation frequency of the source intensity and v is the speed of light in the tissue.

#137543 - $15.00 USD Received 2 Nov 2010; revised 3 Feb 2011; accepted 4 Feb 2011; published 11 Feb 2011

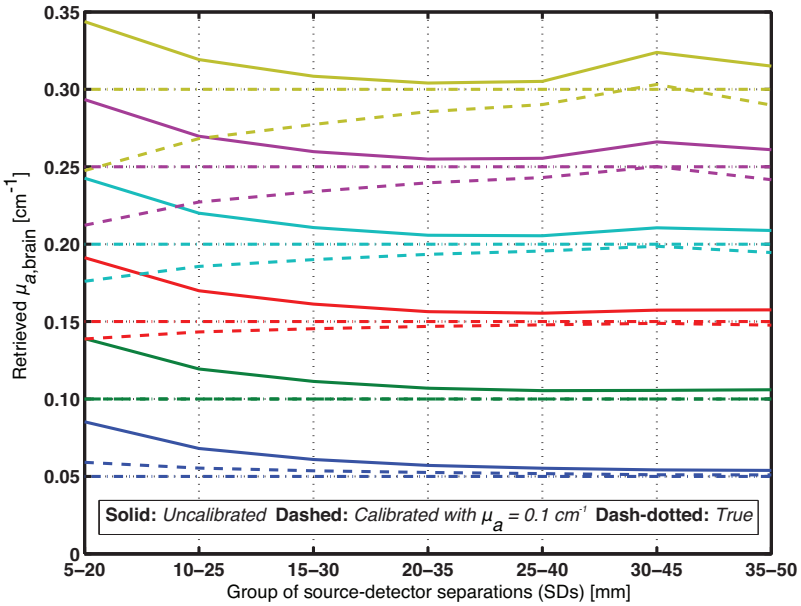

Fig. 2. Retrieved absorption coefficients of a homogeneous slab (calibrated with $\mu_a = 0.1\,\mathrm{cm}^{-1}$). Calibrated (dashed) and uncalibrated (solid) are compared to true (dash-dotted) values with respect to SDs for different homogeneous coefficients of absorption [cm^{-1}]: 0.05 (blue); 0.10 (green); 0.15 (red); 0.20 (cyan); 0.25 (magenta); 0.30 (yellow).

2.4. Calibration method

The intensity and phase signals were calibrated prior to recovery. The calibration method implemented [18] is the same as that used in experimental data acquisition [10, 11]. It calculates corrective factors for the DC, AC, and phase of the light source [41], based on measurements in a phantom block of known optical properties. In this study, we modeled the measurements of the calibrated block with MC simulations in a large homogeneous slab imitating a semi-infinite medium. The dimensions of the slab were $18 \times 18 \times 10\,\mathrm{cm}^3$ and its optical properties set to $\mu_a = 0.1\,\mathrm{cm}^{-1}$, $\mu_s' = 10\,\mathrm{cm}^{-1}$, $g = 0.01$, and $n = 1.3$. The corrective calibration factors $(I_{\mathrm{AC}}^{\mathrm{calib}}, \varphi^{\mathrm{calib}})$ were calculated so that the slopes of intensity and phase simulated from the slab $(I_{\mathrm{AC}}^{\mathrm{slab}}, \varphi^{\mathrm{slab}})$ matched the theoretical ones:

$$I_{\mathrm{AC}}^{\mathrm{calib}} = I_{\mathrm{AC}}^{\mathrm{theo}} / I_{\mathrm{AC}}^{\mathrm{slab}} \qquad \text{with} \qquad I_{\mathrm{AC}}^{\mathrm{theo}} = \exp\left(d\, S_{\mathrm{AC}}^{\mathrm{theo}}\right) / d^2 \tag{3}$$

and

$$\varphi^{\mathrm{calib}} = \varphi^{\mathrm{theo}} - \varphi^{\mathrm{slab}} \qquad \text{with} \qquad \varphi^{\mathrm{theo}} = d\, S_{\varphi}^{\mathrm{theo}} \tag{4}$$

where the expressions $S_{\mathrm{AC}}^{\mathrm{theo}}$ and $S_{\varphi}^{\mathrm{theo}}$ are detailed in [42]. These calibration factors were then applied to noisy intensity and phase signals from the simulated head data. Finally, Eq. (2) were used to recover the values of optical properties.

We show in Fig. 2 the effect of the calibration procedure in the homogeneous slab itself. In particular, the calibration helps reducing large errors due to the FD-MD approximations at short SDs. However the effect of the absorption coefficient of the calibration block appears clearly. When the absorption coefficient of the measured sample is close to that of the calibration block ($0.1\,\mathrm{cm}^{-1}$, green set), the calibration process improves the results. When the absorption of

#137543 - $15.00 USD Received 2 Nov 2010; revised 3 Feb 2011; accepted 4 Feb 2011; published 11 Feb 2011

the medium is much higher than that of the calibration block (e.g. $0.3\,\mathrm{cm}^{-1}$, yellow set) the calibration process results in an underestimation of the absorption in the medium.

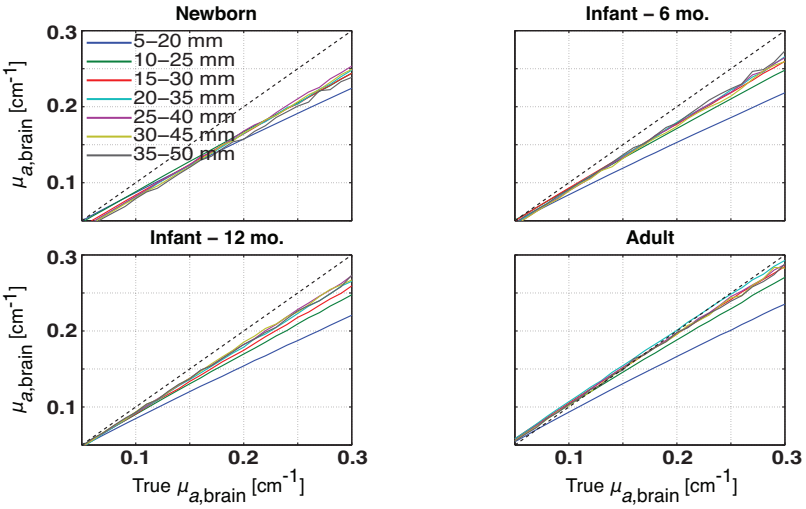

Fig. 3. Estimated $\mu_{a,\mathrm{brain}}$ when the head is treated as a homogeneous medium, i.e. when $\mu_{a,\mathrm{superf}} = \mu_{a,\mathrm{brain}} = [0.05, 0.06, \ldots, 0.29, 0.3]\,\mathrm{cm}^{-1}$. For each sub-figure, solid lines represent the 7 groups of SDs used in the estimation (legend is shown in top left sub-figure) and dotted lines represent the 1-ratio between estimated and true brain absorption values.

3. Results

3.1. Homogeneous head model

To separate the errors due to the diffusion approximation, finite geometry, and curvature from the errors due to the layered structure of the head, we first treated the head as a homogeneous medium by setting equal the superficial and brain absorptions, i.e. $\mu_{a,\mathrm{superf}} = \mu_{a,\mathrm{brain}} = [0.05, 0.06, \ldots, 0.29, 0.3]\,\mathrm{cm}^{-1}$. In Fig. 3, each graph presents the retrieved brain absorption for the 7 sets of SDs. The adult model shows better estimate than the young models. This is due to the stronger head curvature for the newborn and infants. In addition, all estimations at 5–20 mm are less accurate because of the diffusion approximation utilized in the FD-MD formulation [41].

In Fig. 4, retrieved absorption coefficients and standard deviation due to experimental noise are shown for three specific cases when $\mu_{a,\mathrm{superf}} = \mu_{a,\mathrm{brain}} = [0.05, 0.15, 0.3]\,\mathrm{cm}^{-1}$. While the retrieved values improve with longer SDs, the uncertainty increases due to decreasing signal to noise ratio. In addition, the underestimation of retrieved absorption coefficient for $\mu_a = [0.15, 0.3]\,\mathrm{cm}^{-1}$ is due to the unmatched calibration medium (calibration $\mu_a = 0.1\,\mathrm{cm}^{-1}$).

Figure 5 presents averages and standard deviations of the retrieved $\mu_{a,\mathrm{brain}}$ over 26 combinations of $\mu_{a,\mathrm{superf}} = \mu_{a,\mathrm{brain}} = [0.05, 0.06, \ldots, 0.29, 0.3]\,\mathrm{cm}^{-1}$. In newborn and infants, the errors vary between 14–21% and 7–20%, respectively, and decreases to 3–14% for the adult head model. At very short distances (5–20 mm), the error is large for all ages (15–20%) due to the non-validity of the diffusion approximation. At long distances, the error decreases down to less than 5% for the adult head, while the stronger curvature of the head is responsible for additional errors in the case of newborn and infants.

#137543 - $15.00 USD Received 2 Nov 2010; revised 3 Feb 2011; accepted 4 Feb 2011; published 11 Feb 2011

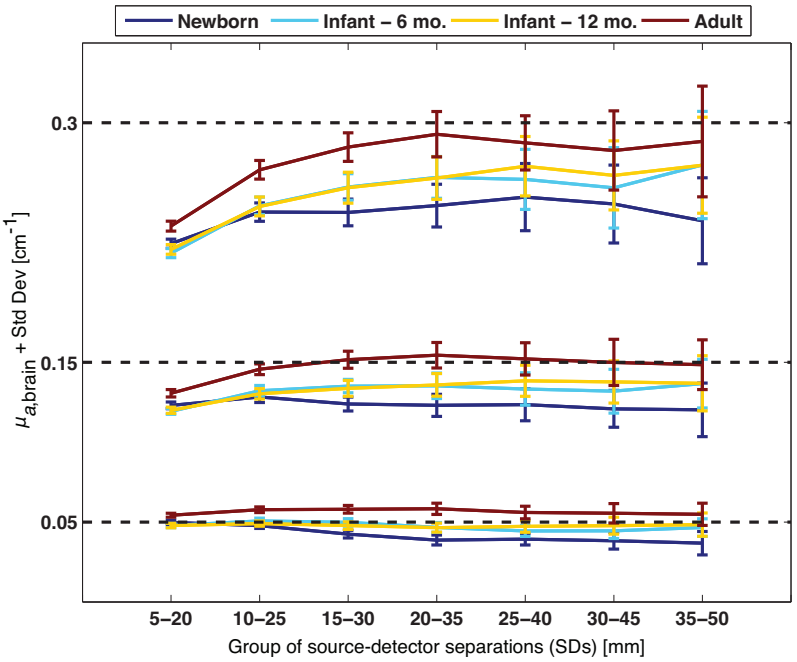

Fig. 4. Uncertainty and retrieved absorption for three particular cases of the homogeneous head: $\mu_{a,\text{superf}} = \mu_{a,\text{brain}} = [0.05, 0.15, 0.3]\,\text{cm}^{-1}$ for the 7 sets of SDs.

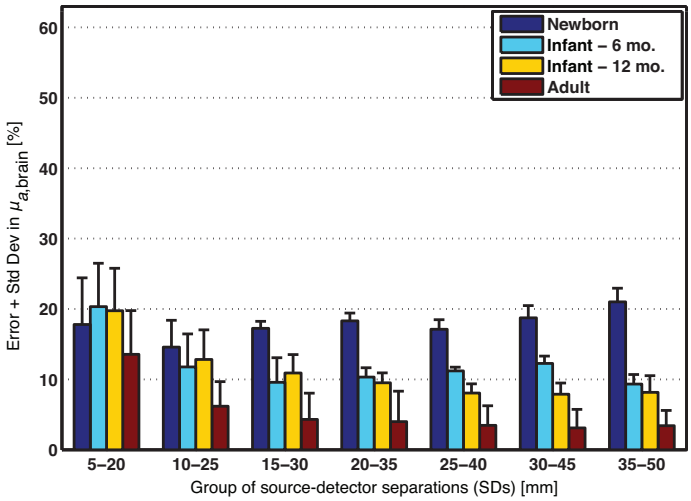

Fig. 5. Averages and standard deviations of the relative error on retrieved $\mu_{a,\text{brain}}$ over 26 combinations of head absorption $[0.05, 0.06, \ldots, 0.29, 0.3]\,\text{cm}^{-1}$, for the 7 sets of SDs.

#137543 - $15.00 USD Received 2 Nov 2010; revised 3 Feb 2011; accepted 4 Feb 2011; published 11 Feb 2011

3.2. *Two-tissue head model*

Figure 6 depicts the evolution of the recovered brain absorption values as a function of true absorption for the 7 groups of SDs in all head models (row-wise) treated as a two-tissue structure. The superficial absorption coefficient $\mu_{a,\text{superf}}$ was set successively to 0.1 and 0.2 cm^{-1} (column-wise). In each sub-figure, the dotted line corresponds to the true brain absorption, while the dash-dotted line identifies the superficial absorption. Solid curves represent the 7 groups of SDs.

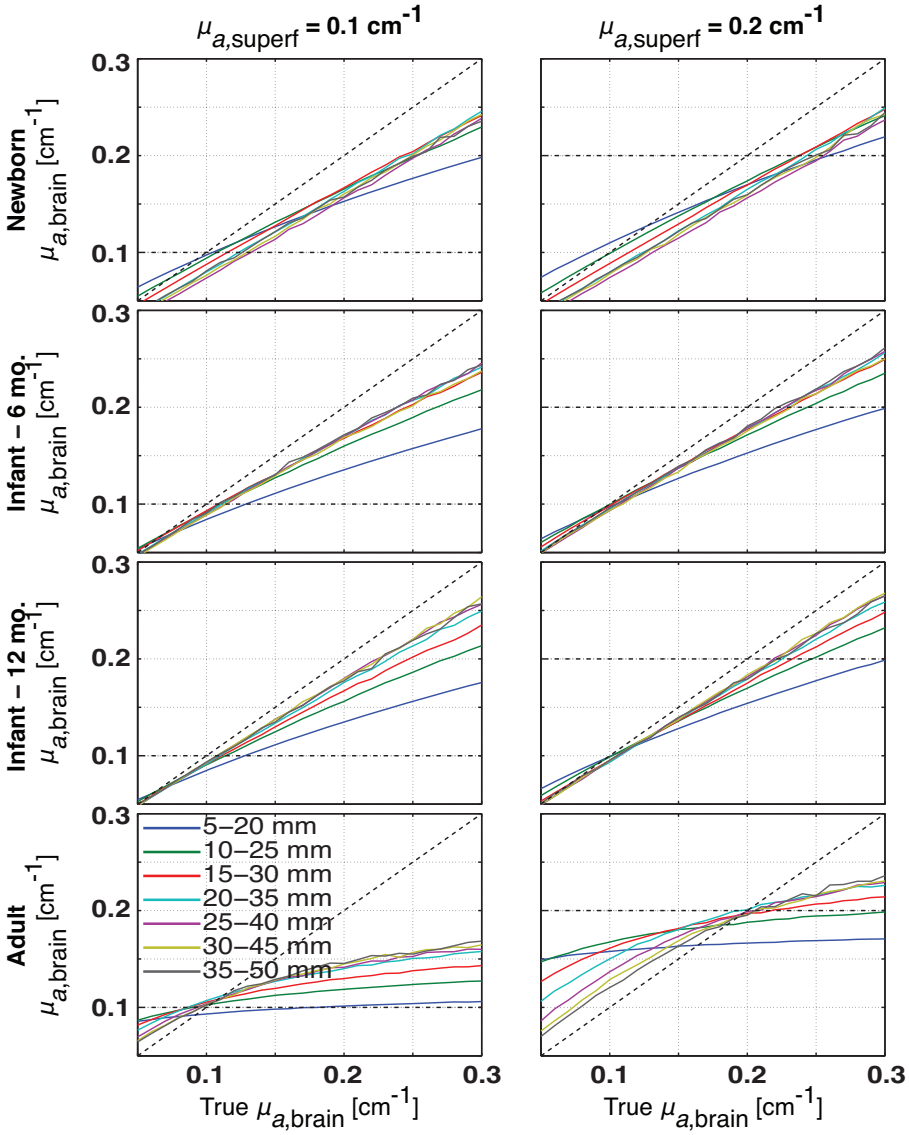

Fig. 6. Brain absorption coefficients $\mu_{a,\text{brain}}$ estimated across subject age (row-wise) and for two values of superficial absorption $\mu_{a,\text{superf}} = [0.1, 0.2]\,\text{cm}^{-1}$ (column-wise). For each sub-figure, solid lines represent the 7 groups of SDs used in the estimation (legend is shown in bottom left sub-figure), dotted lines represent the 1-ratio between estimated and true brain absorption values and dash-dotted lines represent the superficial absorption.

#137543 - $15.00 USD Received 2 Nov 2010; revised 3 Feb 2011; accepted 4 Feb 2011; published 11 Feb 2011

The effect of the superficial layer is to pull the recovered absorption value of the brain towards the superficial absorption value, especially at short SDs and for the adult case. Because of the specific sets of optical properties we chose, this selection leads to a generally weaker than true value $\mu_{a,\text{brain}}$, especially for high brain absorption coefficients. The three young head models present similar brain absorption estimations, mostly underestimated, probably due to the head's curvature. The adult head presents a less precise estimation including over- and underestimations, due to the large thickness of the superficial layer which contaminates the signal especially at short SDs.

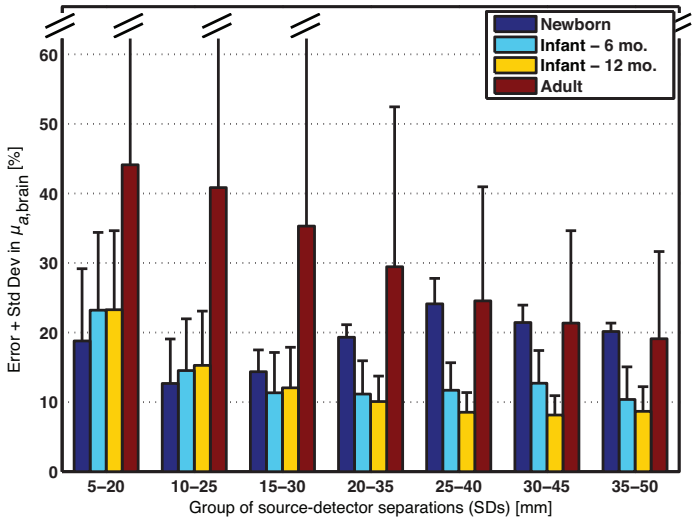

Fig. 7. Two-tissue head model: averages and standard deviations of the relative error in retrieved $\mu_{a,\text{brain}}$ over 52 combinations of $\mu_{a,\text{superf}} = [0.1, 0.2]\,\text{cm}^{-1}$ and $\mu_{a,\text{brain}} = [0.05, 0.06, \ldots, 0.29, 0.3]\,\text{cm}^{-1}$ for the 7 sets of SDs.

Figure 7 shows the average error at each age for all SDs groups, over 52 absorption combinations covering the whole range of coefficients for the brain ($\mu_{a,\text{brain}}$ between 0.05 and 0.3 cm^{-1} in steps of 0.01 cm^{-1}) and the superficial layer ($\mu_{a,\text{superf}} = 0.1$ or 0.2 cm^{-1}).

For the newborn, the optimal SDs group is 10–25 mm and shows a relative error of $12 \pm 6\%$. The 6 and 12 month old infants present a similar trend: the relative error is about $10 \pm 5\%$ for all SDs groups, except for the two shortest (5–20 and 10–25 mm). For both infants, the optimal SDs group can be selected from the five longest SDs (from 15–30 to 35–50 mm), since the error is minimized and shows similar values. The adult head shows the highest relative error for almost all SDs groups (with certain combinations of optical properties yielding errors of more than 80%). The optimal SDs group is reached at 35–50 mm with a corresponding error of $19 \pm 13\%$.

The effect of the scattering coefficient was investigated by modifying the value in the superficial layer to $\mu'_{s,\text{superf}} = 5\,\text{cm}^{-1}$. The relative error decreases in the newborn (ranging from 6 to 19%) and infant models (2–10%) for all SDs except the shortest group (5–20 mm), and slightly increases in the adult head (from 26 to 45%) for almost all groups (except for 10–25 and 15-30 mm). Again, this is probably due to the thicker superficial layer in the adult model that causes a stronger error in μ'_s translating through cross-talk in higher error in μ_a.

The same analysis was performed with the adult model in which a large vessel was introduced. Relative errors and standard deviations [%] for the 7 SDs (from 5–20 to 35–50 mm) are

#137543 - $15.00 USD Received 2 Nov 2010; revised 3 Feb 2011; accepted 4 Feb 2011; published 11 Feb 2011

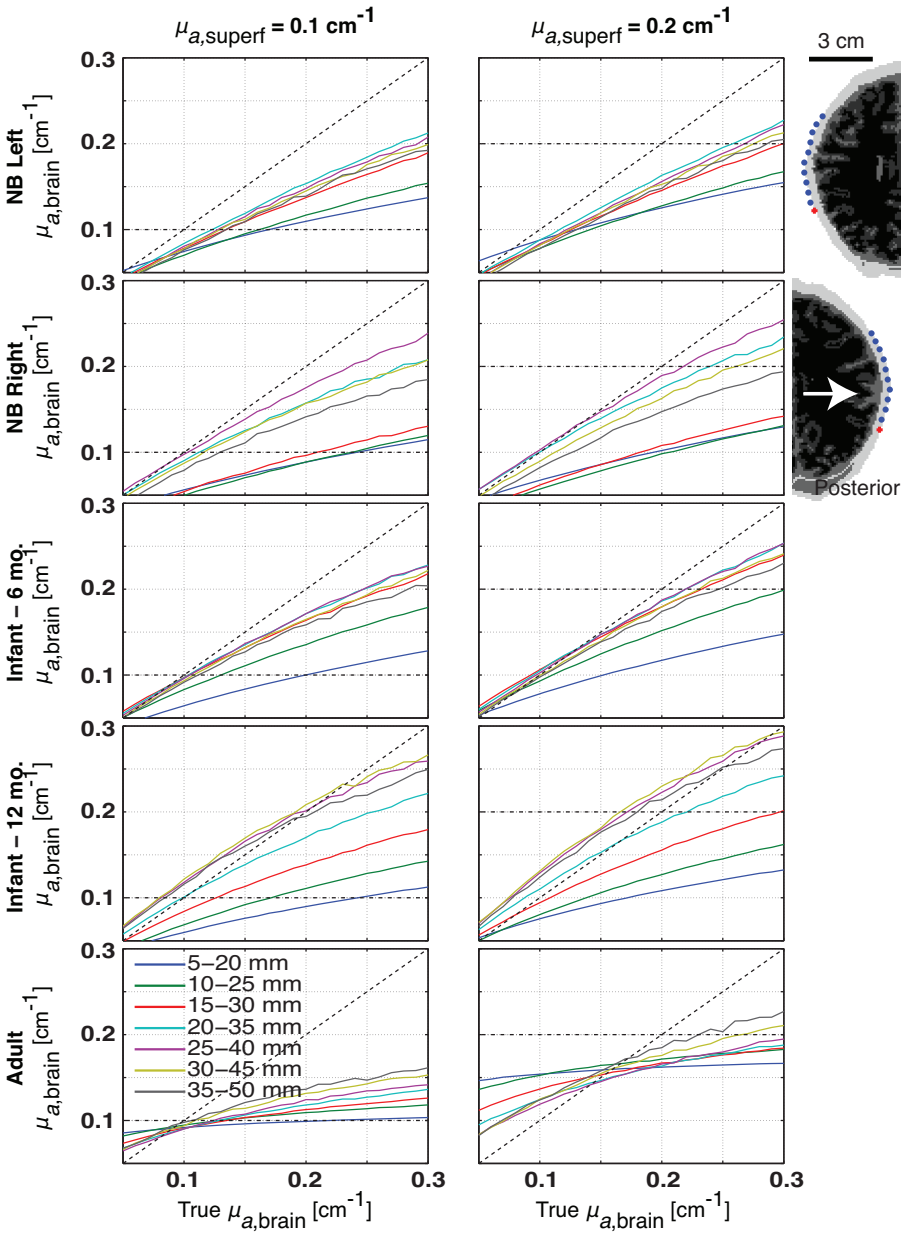

Fig. 8. Brain absorption coefficients $\mu_{a,\text{brain}}$ estimated across subject age (row-wise) and for two values of superficial absorption of $\mu_a = [0.1, 0.2]\,\text{cm}^{-1}$ (column-wise) when the CSF tissue is taken into account. For each sub-figure, solid lines represent the 7 groups of SDs used in the estimation (legend is shown in bottom left sub-figure), dotted lines represent the 1-ratio between estimated and true brain absorption values and dash-dotted lines represent the superficial absorption. Note the presence of the axial slice of the newborn (NB) left and right hemispheres superimposed with the optical probe.

#137543 - $15.00 USD Received 2 Nov 2010; revised 3 Feb 2011; accepted 4 Feb 2011; published 11 Feb 2011

the following: 51.6 ± 58.2; 48.3 ± 53.9; 35.4 ± 33.4; 26.3 ± 18.1; 23.7 ± 14.7; 22.0 ± 14.5; 19.2 ± 13.2. The error is higher than the case without inhomogeneity in the first 3 groups and then similar for the next 4 groups. The contamination of the shortest estimations is related to the length of the vessel (3 cm) which was located around the beginning of the probe where the light source is positioned. This type of inhomogeneity can be detected experimentally, and data automatically discarded, because of the corresponding low correlation factor r^2 of the linear fitting process from Eq. (1).

3.3. Three-tissue head model

We investigated the influence of the CSF structure by setting its optical properties to low absorption and scattering values: $\mu_a = 0.04\,\mathrm{cm}^{-1}$ and $\mu_s' = 0.1\,\mathrm{cm}^{-1}$. The two hemispheres (left and right parietal) of the newborn were studied, because the right hemisphere possessed a thick "pocket" of CSF located underneath the optical probe (white arrow on the axial slice of the second row in Fig. 8), while the left hemisphere possessed a "normal" amount of fluid.

Figure 8 shows retrieved $\mu_{a,\mathrm{brain}}$ with respect to true values for the 7 groups of SDs. The first two columns correspond to $\mu_{a,\mathrm{superf}}$ set to 0.1 and $0.2\,\mathrm{cm}^{-1}$, respectively. The third column shows an axial slice of the left and right newborn (NB) hemispheres. Each graph was created in the same way as in Fig. 6. Distortion of the value of $\mu_{a,\mathrm{brain}}$ by the superficial layer is similar to the effect observed when ignoring CSF, with the difference that the low absorption of CSF pulls the retrieved $\mu_{a,\mathrm{brain}}$ to lower values than in the previous case.

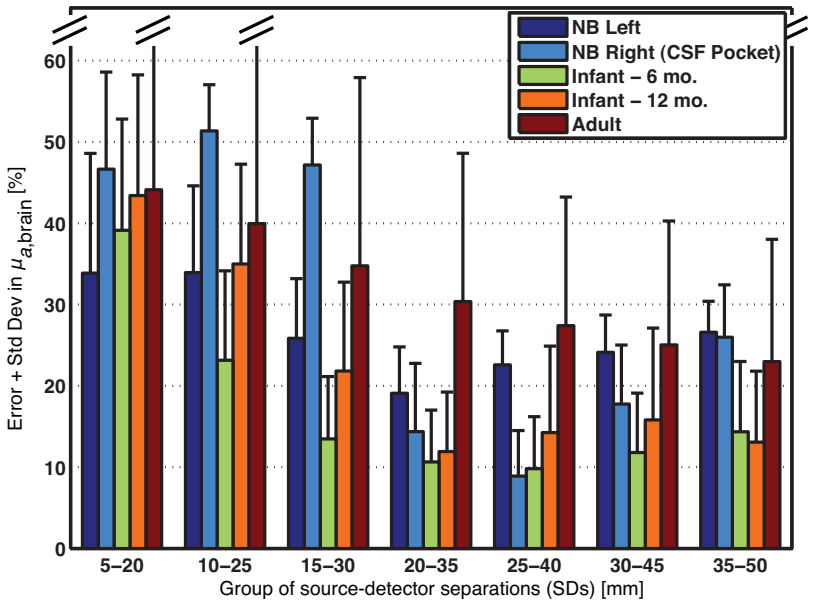

Fig. 9. Three-tissue head model: averages and standard deviations of the relative error on retrieved $\mu_{a,\mathrm{brain}}$ over 52 combinations of $\mu_{a,\mathrm{superf}} = [0.1, 0.2]\,\mathrm{cm}^{-1}$ and $\mu_{a,\mathrm{brain}} = [0.05, 0.06, \ldots, 0.29, 0.3]\,\mathrm{cm}^{-1}$ for the 7 sets of SDs.

For the newborn, the estimations computed at shorter SDs in the left hemisphere are less distorted than those estimated in the right hemisphere. This is due to the large volume of CSF in the vicinity of the optical probe. The clear pocket of CSF contributes to modification of the signal through the combined effects of very low absorption and scattering. In general, short SDs groups, from 5–20 to 15–30 mm, are poorly estimated for all head models.

#137543 - $15.00 USD Received 2 Nov 2010; revised 3 Feb 2011; accepted 4 Feb 2011; published 11 Feb 2011

Figure 9 shows the averages of the relative errors and standard deviations in percentage [%] of $\mu_{a,\text{brain}}$ for all 52 combinations of optical properties of brain and superficial tissues. The error rises to a maximum of 51% for the newborn right hemisphere, mostly due to the effect of the CSF pocket. For the newborn left hemisphere, the optimal set of SDs is 20–35 mm and the error is 19 ± 5%. Decreasing error with increasing SDs is still true for the adult model to a slightly higher extent. The distinction between 6 and 12 month old infants is more visible than in the case without CSF. The 12 month old infant shows less accurate estimations for almost all SDs because of the thicker superficial layer. In both cases, optimal SDs are between 20–35 and 30–45 mm, where the errors is less than 16 ± 10%. For the adult, the longest SDs group (35–50 mm) is needed to minimize the error to a value of 23 ± 15%.

The influence of the CSF was also studied for a superficial scattering coefficient of 5 cm^{-1}. For all head models, the error at 5–20 mm increases. For the newborn, both hemispheres show lower errors (ranging from 7 to 45%) with the lower scattering coefficient (except for 25–40 mm in the right hemisphere: error increased to 13%). In the case of the 12 mo. old infant, the error increases from 15 to 61% (except for 10–25 and 15–30 mm: down to 30 and 16%, respectively) while decreases to a minimum of 6 and 25% in the 6 mo. old infant and adult, respectively (data not shown).

4. Discussion

4.1. Effect of the curvature

Generally, the estimations computed at longer distances are strongly affected by head curvature in young subjects. The fitted slopes from Eq. (1) deviate from the theoretical slopes computed with the flat calibration slab. In practice, measurements on a curved region of the head lead to a non-linear variation of the phase and intensity with source-detector separation. This error is easily visible in the raw data and such data can be objectively discarded, as performed in [10–12].

4.2. Effect of the superficial layer

When modeling the head with two layers, the adult model shows larger errors for almost all SDs groups. This is due to the thicker layer of extra-cerebral tissue in adults. Even at the optimal SD separations, the brain absorption is still estimated with 19% error, compromising the validity of longitudinal or cross-sectional studies. Implementing more complex models of the head that incorporate the layered structure more realistically can help solve this issue.

4.3. Effect of the CSF layer

In newborn, we studied one location where a thick region of CSF was located directly underneath the optical probe, hindering the recovery of brain optical properties at short distances (from 5–20 to 15–30 mm). This lateral "CSF pocket" could have been produced by the positioning of the head during the MR scan. At this age, the skull is very flexible and the CSF can be distributed according to the pressure applied on the surface of the head. Even though the skull layer is very thin in neonates, facilitating the measurement of brain absorption coefficients, the relatively thick CSF layer can affect the performance of the method. For the adult head model, results with and without CSF were very similar. The 6 and 12 month old infants often yield more accurate estimates than the newborn, with and without the optical properties of the CSF. This is probably due to the description of the CSF, the size of the superficial layer (scalp and skull) and the head size of the infant models. This suggests that the dominant error is not related to the CSF compartment.

#137543 - $15.00 USD Received 2 Nov 2010; revised 3 Feb 2011; accepted 4 Feb 2011; published 11 Feb 2011

4.4. *Effect of the scattering coefficient*

Surprisingly, decreasing the scattering coefficient of the extra-cerebral tissue from 10 to 5 cm^{-1} produced better results for the newborn and infants, which can probably be explained by compensatory errors. On the contrary, it deteriorated the estimation for the adult at almost all SDs groups. A more extended study of this effect should yield more robust conclusions.

4.5. *Large vessel, hair obstruction and extra-cerebral inhomogeneities*

The presence of extra-cerebral inhomogeneities such as vessel or hair is generally uncontrolled and their locations are unknown except if angiography data are accessible. We showed how such strongly absorbing local structure can affect the retrieved absorption, but also how it deteriorates the linear fit of the slope. In practice, such data are easily rejected based on objective criteria employed in experimental studies [10–12], and the probe is slightly moved to avoid the inhomogeneities.

4.6. *Derived physiological variables*

Computation of baseline hemoglobin concentrations from the retrieved absorption coefficients allows clinical investigations [10–12] and derivation of physiological variables such as cerebral blood volume (CBV) and oxygen saturation (StO_2). For the typical wavelengths of 690 and 830 nm, the propagation of the error from retrieved absorption to hemoglobin concentration was computed [43] for the newborn and the adult using specific extinction coefficients [39]. For the newborn, the typical error of 12% in absorption propagates into an error of 17, 20 and 11% for HbO, HbR and HbT, respectively. For the adult, the minimal error of 19% corresponds to 27, 31 and 17% for HbO, HbR and HbT, respectively. The propagation of the error for CBV has the same rate than HbT while the error for StO_2 propagates to 8% and 13% for the newborn and adult, respectively.

4.7. *Error arising from the diffusion approximation*

The FD-MD method is based on the diffusion approximation and its formulation relies on additional approximations [41]. These approximations lead to errors in the recovered optical properties, even for a large homogeneous slab and especially at short SDs (Fig. 2). Typically, the recovered μ_a for a homogeneous slab is overestimated by 20% at short SDs (5–20 mm), but only 5% at large SDs (from 25–40 to 35–50 mm) when no calibration is applied: this method favors long distance estimations because it neglects terms of order greater or equal to 1 in the Taylor development [41]. Adequate calibration of the data reduces this error.

4.8. *Error arising from the finite geometry*

The FD-MD method also considers that the light is propagating in a semi-infinite medium. This assumption is less true for the newborn model since the head size is markedly smaller than the adult (Fig. 1). The error related to the finite geometry is higher in the newborn estimations compared to the three other head models.

4.9. *Limitations*

All head models originated from anatomical MRI data sets and were created with a semi-automatic tissue segmentation procedure. This method enabled us to simulate light propagation with Monte Carlo methods in a voxel-wise approach. However, since each voxel has a discrete 3D resolution of $1\,mm^3$ for each head model, the boundaries of all segmented tissues are represented non-uniformly, especially curved layers. The number of photons detected on the skin

#137543 - $15.00 USD Received 2 Nov 2010; revised 3 Feb 2011; accepted 4 Feb 2011; published 11 Feb 2011

depends strongly on local geometry, i.e. on the position of the detector with respect to the voxelization defining the local curvature. This local geometry can be slightly irregular across head models, which can then lead to under- or overestimated fluences.

Also, a consequence of voxelization and voxel size is imprecision of the SD separations. The distances *d* used in the fit procedure are the theoretical distances used with the calibration slab phantom, which correspond to the set $[5, 10, \ldots, 50]$ mm. However, the "real", or simulated, distances for all head models are those determined by the voxel difference between the source and detector positions that belong to the skin. These distances can differ by 0.1 to 0.5 mm from those used in the flat slab, where the curvature is null. These artefacts are higher for the newborn than the adult because the neonate head presents more curvature poorly sampled by the 1 mm^3 voxels . However, these artefacts are due solely to the simulation process, and are not representative of any errors observable in experimental studies. We reduced these errors by averaging multiple probe locations. These errors in our method set the minimum on the accuracy with which absorption coefficients can be recovered.

4.10. Future work

In the present study, the effect of the heterogeneous anisotropy across the head [44] was not investigated. Future simulations could incorporate realistic tissue-dependent anisotropy factors.

Future simulations at intermediate ages are necessary to determine the age limit at which the FD-MD method becomes less accurate than 10 or 15%. Also, more accurate segmentation algorithms can provide improved head models and thus better estimates for the young population [45]. In addition, the study of the FD-MD method performance in premature neonates will also be crucial in order to characterize the effects of the thick CSF layer in this population.

5. Conclusion

In this study, we investigated the performance of the FD-MD method when measuring the brain optical absorption at different ages from newborn to adult. In the neonate and infants, the error is dominated by the head curvature and can be minimized around 10–15%. At these ages, the effect of the extra-cerebral layer is small and visible only at short SDs. On the contrary, it becomes dominant in the adult case because of the larger thickness of the scalp and skull. In adults, the strong contamination by the superficial layers leads to both under- and overestimations of the brain absorption coefficient, depending on the relative absorption values assigned to the intra- and extra-cerebral tissues. Not only is the mean error much larger (above 20%) than in the younger head models, but there is a large variability of this error across sets of optical properties. This argument strongly suggests the use of a two- [34] or three-layer [35] model to minimize the deterioration produced by the extra-cerebral layers. In all cases, measurements at 5 mm should be avoided because of the diffusion approximation.

Acknowledgments

The authors thank Myong-Sun Choe (CHB) and Lilla Zollei (MGH). This work was supported by the NIH/NICHD grants # R01-HD042908 and R21-HD058725, the NIH/NCRR grant # P41-RR14075 and the Fonds Québécois de la Recherche sur la Nature et les Technologies (FQRNT-B3, Canada).

#137543 - $15.00 USD Received 2 Nov 2010; revised 3 Feb 2011; accepted 4 Feb 2011; published 11 Feb 2011